Electronic structure, magnetic structure, and metal-atom site preferences in CrMnAs

by

Laura Christine Lutz

A thesis submitted to the graduate faculty

in partial fulfillment of the requirements for the degree of

MASTER OF SCIENCE

Major: Materials Science and Engineering

Program of Study Committee:

Gordon J. Miller, Co-major Professor

Scott Beckman, Co-major Professor

Ralph Napolitano

Iowa State University

Ames, Iowa

2013

Copyright © Laura Christine Lutz, 2013. All rights reserved.

TABLE OF CONTENTS

LIST OF TABLES iii

LIST OF FIGURES iv

ACKNOWLEDGEMENTS v

ABSTRACT vi

CHAPTER 1. INTRODUCTION 1

Introduction to the materials 3

The structure and properties of CrMnAs 3

Antiferromagnetism of Cr_2As and Mn_2As 7

Introduction to the computational methods 10

VASP 10

TB-LMTO-ASA 10

Other software tools 11

Goals 11

CHAPTER 2. RESULTS 12

Total energy of six-atom unit cell 12

Total-energy calculations 14

LDA band structure, density of states, and COHP analysis 18

Total energy of 12-atom supercell 25

CHAPTER 3. CONCLUSION 33

BIBLIOGRAPHY 37

LIST OF TABLES

Table 1.1 ICSD structural data that appear to be inaccurate. 5

Table 1.2 Structural data from (*1*). 6

Table 1.3 ICSD structural data for CrMnAs, based on work of Fruchart (*2*). 6

Table 2.1 LDA total energies of three colorings of chemical unit cell. 15

Table 2.2 LSDA energies and magnetizations with five magnetic orderings. 15

Table 2.3 LSDA total energies of chemical unit cell with structural relaxation. 17

Table 2.4 Number of bands below Fermi energy at high-symmetry k-points. 19

Table 2.5 –ICOHP values calculated with LDA. 24

Table 2.6 LSDA total energies of 12-atom supercell with ten magnetic orderings. 27

Table 2.7 Magnetic moments found with LSDA on 12-atom supercell. 28

Table 2.8 Structural relaxation on AF3 case. 30

Table 2.9 Structural relaxation on AF8 case. 31

Table 2.10 LSDA total energies of AF3 and AF8 with different geometries. 32

LIST OF FIGURES

Figure 1.1 Chemical and magnetic unit cells. 2

Figure 1.2 The atomic structure of tetragonal CrMnAs. 4

Figure 1.3 Exaggerated view of two structures for CrMnAs listed in ICSD. 4

Figure 1.4 The previously reported magnetic structure of CrMnAs. 8

Figure 1.5 The magnetic structures of Cr_2As, CrMnAs, and Mn_2As. 9

Figure 2.1 Possible colorings that preserve symmetry of chemical unit cell. 12

Figure 2.2 Possible magnetic orderings that preserve symmetry. 14

Figure 2.3 Brillouin zone of space group P4/nmm. 18

Figure 2.4 LDA band structure with Cr at M(I). 19

Figure 2.5 LDA band structure with Mn at M(I). 20

Figure 2.6 LDA densities of states. 21

Figure 2.7 LDA partial densities. 22

Figure 2.8 LDA COHP with 100% of Cr at site M(I). 23

Figure 2.9 LDA COHP with 100% of Mn at site M(I). 23

Figure 2.10 Ten antiferromagnetic orderings of 12-atom supercell. 26

Figure 2.11 LDA and LSDA total energies. 28

Figure 2.12 Overview of lowest-energy orderings. 29

ACKNOWLEDGEMENTS

This work would not have been possible without the advice and assistance I received from Gordie Miller and from all the members of the Miller and Corbett research groups. Particular thanks are due to Yuemei Zhang: for teaching me the computational techniques used here, for providing advice on how to move the project forward, and for identifying crucial errors in earlier drafts of this work. Her assistance, particularly in noting the discrepancy between ICSD entries discussed in subsection 1.1.1, was invaluable to me. Financial support for this work was generously provided by the National Science Foundation, Materials World Network (NSF DMR 12-09135).

ABSTRACT

Density functional theory was used to examine stoichiometric CrMnAs, one of a class of $3d$-metal arsenides that exhibit cooperative magnetic ordering. CrMnAs is a tetragonal structure with two inequivalent metal sites: M(I), which is tetrahedral coordinate, and M(II), which is square pyramidal coordinate. CrMnAs thus presents a "coloring problem," the question of how the two types of metal atoms are distributed between the two types of metal sites. Previous diffraction studies have determined that CrMnAs is antiferromagnetic with the M(I) site primarily occupied by Cr.

TB-LMTO-ASA local density approximation (LDA) calculations showed indications of instability in the nonmagnetic structure, which could be resolved either by structural distortion or by spin polarization. LDA crystal orbital Hamilton population (COHP) curves were used to predict the nature of particular direct-exchange interactions upon spin polarization. Spin-polarized total energy calculations were performed using VASP with the generalized gradient approximation (GGA).

The lowest-energy structure had Mn at the M(I) site and a different antiferromagnetic ordering than previously observed. The structure with the second-lowest calculated total energy also had Mn at M(I). Next lowest were four structures with Cr at M(I), including the experimentally observed structure. Those four had calculated total energies ranging from 154.2 to 167.8 meV/f.u. higher than the lowest-energy case. The number of possible structures with small energy differences suggests that the observed magnetic ordering and coloring may be due to entropy rather than reflecting a true electronic ground state.

CHAPTER 1. INTRODUCTION

Cooperative magnetic ordering phenomena such as ferromagnetism, antiferromagnetism, and ferrimagnetism have been studied for more than a century, but such phenomena are relatively rare among materials in general (*3*). With the rise of technology that depends on the magnetic properties of materials, particularly electronic storage media, the development of compounds with tailored magnetic properties has become increasingly important (*4*, *5*). The relationship between composition, structure, and magnetic properties is not straightforward, however, and discovery of new compounds has so far demanded trial and error (*6*). Computational insights into the origins of cooperative magnetic phenomena thus have the potential to become valuable heuristics for synthetic research. Declining cost and increasing speed of computation also increase the appeal of such approaches, as more solid-state scientists have access to electronic structure calculations.

In general, cooperative magnetic phenomena arise from some sort of coupling interaction between magnetic moments in a material (*7*). These phenomena are classified according to the resulting long-range patterns in the magnetic moments. Perhaps the most familiar is ferromagnetism, in which all atomic magnetic moments share the same sign, resulting in a net magnetization that persists in the absence of an external field. Antiferromagnetism is characterized by an ordered array of magnetic moments with alternating signs that results in zero net magnetization. In ferrimagnetism, one or more chemical species have magnetic moments with opposite signs but different magnitudes, resulting in an intermediate net magnetization. A magnetic material will also have a magnetic ordering temperature, called a Curie temperature for ferromagnetism and a Néel temperature for antiferromagnetism and ferrimagnetism, above which the material behaves paramagnetically.

All three types of magnetic order can be identified in bulk materials by measuring mag-

netization as a function of temperature and external field, but bulk magnetization does not provide enough information to distinguish particular magnetic orderings within each type. For a simple example, consider a binary compound with the chemical structure shown in Figure 1.1a. Figure 1.1b and Figure 1.1c show two different possible magnetic orderings, but both are antiferromagnetic. These examples illustrate another important consideration about antiferromagnetism and ferrimagnetism: The periodicity of the magnetic moments may not be equal to the periodicity of the chemical structure. The supercell that captures the full symmetry of the magnetic ordering is called the magnetic unit cell. In Figure 1.1b, the magnetic unit cell is equal to the chemical unit cell, but in Figure 1.1c, it is doubled along the vertical axis. To experimentally distinguish between such antiferromagnetic cases, diffraction measurements are necessary.

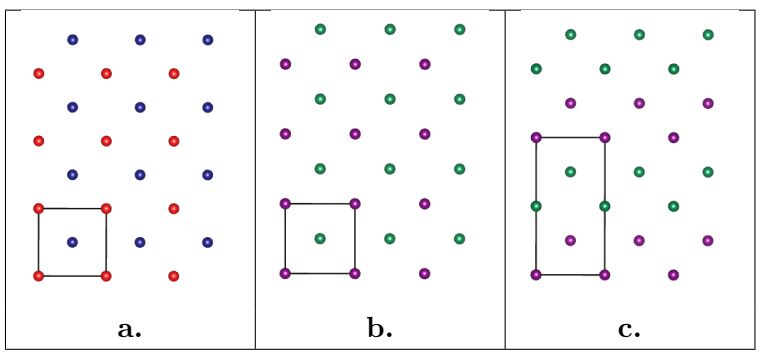

Figure 1.1: a. A possible chemical structure, with red and blue dots representing two chemical species. b. and c. Two possible antiferromagnetic orderings of that chemical structure, with spin-up and spin-down represented by purple and green dots.

Antiferromagnetism has been observed in several tetragonal 3d-metal arsenides of the series $(M_xM'_{1-x})_2As$, including Cr_2As, Mn_2As, Fe_2As, MnFeAs, and CrMnAs (*1*, *2*, *8–18*). These structures are fairly simple, with just six atoms in the chemical unit cell, but they vary in the distribution of moments that leads to their overall antiferromagnetism. This makes those structures an ideal testbed for understanding the electronic origins of cooperative magnetic phenomena. It is hoped that understanding the origins of antiferromagnetism in the 3d-metal arsenides will provide insights that can be applied to more complex compounds that are less amenable to exhaustive ab initio analysis (*6*). The binary M_2As 3d-metal arsenides were the subject of a recent study by members of this research group (*12*), and their research

suggested that, within the series of related compounds, the ground state might be predicted from valence electron count alone. Cr_2As, Mn_2As, and Fe_2As have 17, 19, and 21 valence electrons, respectively. This research extends that study to the ternary compound CrMnAs, which fits between Cr_2As and Mn_2As with 18 valence electrons.

In order to understand the relationship between composition and structure, it is also necessary to consider the "coloring problem," the question of where the atoms are within the structure (*19*). In the case of CrMnAs, the key coloring question is how Cr and Mn are distributed between the two metal sites in the structure. As described below, previous experiments have indicated that both metal sites have mixed occupancy, but with more Cr on one site and more Mn on the other (*1*, *2*, *20*). That site preference may determine, or be determined by, the magnetic ordering, so a complete understanding of the magnetic ordering requires consideration of the coloring.

1.1 Introduction to the materials

1.1.1 The structure and properties of CrMnAs

CrMnAs, like Cr_2As, Mn_2As, and Fe_2As, adopts a tetragonal structure with a 6-atom chemical unit cell, as shown in Figure 1.2. This is the Cu_2Sb-type structure in space group $P4/nmm$ (#129). It has two metal-atom sites, one at Wykcoff site $2a$, labeled M(I), and another at a Wyckoff site $2c$, M(II). The arsenic atoms occupy a different $2c$ site. The M(I) metal atoms are tetrahedrally coordinated by four As atoms, and the M(II) metal atoms are square-pyramidally coordinated by five adjacent As atoms (*13*, *21*, *22*).

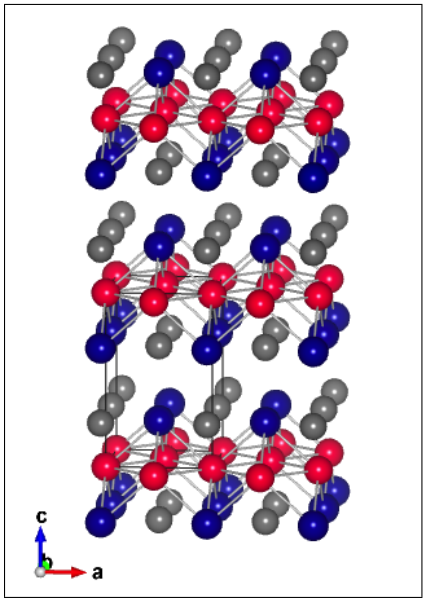

Figure 1.2: The atomic structure of tetragonal CrMnAs. Grey dots represent arsenic, red dots represent the M(I) metal site, and blue dots represent the M(II) metal site. The chemical unit cell is outlined in black.

The Inorganic Crystal Structure Database (ICSD) lists two sets of structural parameters for tetragonal CrMnAs, which differ in the distance of the M(II) and As sites from the M(I) slabs. One ICSD entry, based on a 1966 x-ray diffraction study published by Hollan in 1966 (*23*), places the M(II) atoms closer to the M(I) layers than the As atoms, as in Figure 1.3a. Those data are shown in Table 1.1.

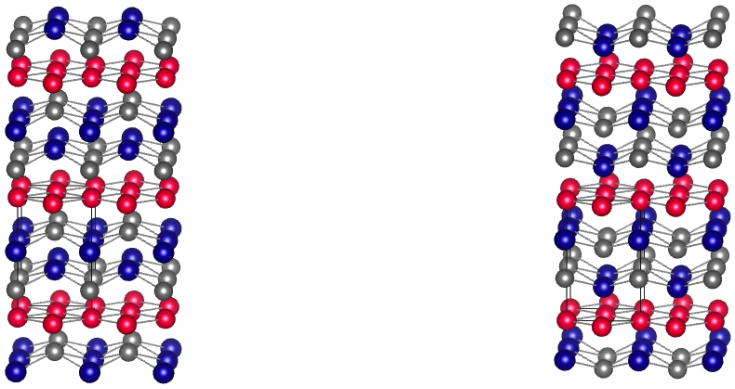

a. M(II) is closer than As to M(I) layer **b.** M(II) farther than As from M(I) layer

Figure 1.3: Exaggerated view of the differences between the two ICSD entries for tetragonal CrMnAs. Red spheres are M(I) atoms, blue are M(II), and grey are As.

Table 1.1: Structural information from ICSD listing for CrMnAs based on Hollan's 1966 study. These structural data, which follow the pattern of Figure 1.3a, do not appear to be accurate.

Lattice parameters:	$a = 3.791$ Å, $c = 6.263$ Å				
Volume:	90.01 Å^2				
	Atom type	Wyckoff site	x	y	z
	M(I)	$2a$	0	0	0
	M(I)	$2a$	0.5	0.5	0
Atom locations:	M(II)	$2c$	0	0.5	0.27
	M(II)	$2c$	0.5	0	0.73
	As	$2c$	0	0.5	0.7
	As	$2c$	0.5	0	0.3

The same ICSD entry also cites a 1978 paper by Yamaguchi and Watanabe, but the data actually given in the 1978 paper instead follow the pattern of Figure 1.3b, with the M(II) atoms farther than the As atoms from the M(I) layers (see Table 1.2). Yamaguchi and Watanabe based their data on neutron diffraction measurements at 120 K, 290 K, and 534 K. The second ICSD entry is based on neutron diffraction studies at 500 K and 550 K that Fruchart and Sénateur presented in 1982 (*2*) (see Table 1.3). The 1982 data also follow the pattern of Figure 1.3b. These two datasets are in general agreement, within only a 2% difference in the a lattice parameter and agreement on the c parameter. The z locations of the M(II) and As sites differ by only 5% and 3%, respectively.

There are several reasons to conclude that the data in Table 1.3, following the scenario depicted in Figure 1.3b, are more reasonable than those in Table 1.1. In the similarly structured binary metal arsenides, Cr_2As, Mn_2As, and Fe_2As, the M(II) sites are farther from the M(I) layers than the As sites are, as in Figure 1.3b (*12*). Analysis by Yuemei Zhang of the diffraction data presented by Yamaguchi and Watanabe in (*1*) agreed with their findings that the diffraction data supported the scenario of Figure 1.3b (*24*). Further, when VASP was used to perform LSDA structural relaxation calculations starting from the data in Table 1.1, the relaxed structures followed the pattern of Figure 1.3b, with the M(II) sites farther from the M(I) layers than the As sites were. The structural data shown in Table 1.3, based on (*2*), were therefore used for the calculations that follow, unless otherwise noted.

Both neutron diffraction studies also reached similar conclusions as to the site preference

Table 1.2: Structural information from Yamaguchi and Watanabe's 1978 study. This structure follows the pattern of Figure 1.3b.

Lattice parameters:	$a = 3.85$ Å, $c = 6.26$ Åat room temperature				
Volume:	92.79 Å^2				
	Atom type	Wyckoff site	x	y	z
	M(I)	$2a$	0	0	0
	M(I)	$2a$	0.5	0.5	0
Atom locations:	M(II)	$2c$	0	0.5	0.673 ± 0.005
	M(II)	$2c$	0.5	0	0.327 ± 0.005
	As	$2c$	0	0.5	0.266 ± 0.005
	As	$2c$	0.5	0	0.734 ± 0.005

Table 1.3: Structural information from ICSD listing for CrMnAs based on Fruchart's 1982 study, which used neutron diffraction at 500 K and 550 K (*2*). This structure follows the pattern of Figure 1.3b. These data were used for the calculations that follow, except where otherwise noted.

Lattice parameters:	$a = 3.758(2)$ Å, $c = 6.259(2)$ Å				
Volume:	88.41 Å^2				
	Atom type	Wyckoff site	x	y	z
	M(I)	$2a$	0	0	0
	M(I)	$2a$	0.5	0.5	0
Atom locations:	M(II)	$2c$	0	0.5	0.6839
	M(II)	$2c$	0.5	0	0.3161
	As	$2c$	0	0.5	0.2798
	As	$2c$	0.5	0	0.7202

of metal atoms in CrMnAs. In 1978, Yamaguchi and Watanabe reported that site M(I) was occupied by $86 \pm 3\%$ Cr and $14 \pm 3\%$ Mn, with the converse on site M(II). A 1999 follow-up by Yamaguchi and others, using the HERMES high efficiency powder neutron diffractometer at the Japan Atomic Energy Research Institute, estimated occupancy at 88% Cr and 12% Mn on site M(I), with the converse on site M(II), for CrMnAs at 445 K (*20*, *25*). In their 1982 report, Fruchart and Sénateur reported 79% Cr and 21% Mn on site M(I), with the converse on site M(II).

Sample preparation is a particular challenge associated with $(Cr_xMn_{1-x})_2As$ measurements, because it can be readily contaminated with Cr_3As_2 and Mn_3As_2 (*23*). Yuzuri reported Cr_3As_2 as ferrimagnetic with a tetragonal structure (*26*), but Watanabe et al. (*15*) found Cr_3As_2 to have a cubic structure. Mn_3As_2 has been observed in both orthorhombic (*27*) and

monoclinic (*28*) phases, and there is also a high-temperature monoclinic $Mn_{2.896(1)}As_2$ phase above about 750 K (*29*, *30*). Yuzuri found a sample of Mn_3As_2 to be ferromagnetic, but it is not clear which crystal structure that sample represented (*30*).

1.1.1.1 Antiferromagnetism of CrMnAs

In contrast to the chemical unit cell, the magnetic unit cell has been found to consist of 12 atoms—the chemical cell is doubled along the c axis (*21*, *25*). The moments of the Cr and Mn atoms are arranged antiferromagnetically both within and between the metal sites, as shown in Figure 1.4 (*25*).[1] The M(I)–M(II) interactions are half ferromagnetic and half antiferromagnetic. As in other M_2As compounds, the M(I) metal generally has a smaller magnetic moment than the M(II) metal (*12*, *15*, *21*).

The two metal sites have been found to have different magnetic ordering temperatures; the material has a Néel temperature of 430 K, which reflects the ordering temperature for site M(II). Another transition has been observed at 290 K, which has been attributed to the ordering of site M(I) (*25*). Below 290 K, the metal atoms have magnetic moments of 0.88 μ_B for site M(I) and 3.14 μ_B for site M(II) (*25*).

1.1.2 Antiferromagnetism of Cr_2As and Mn_2As

Powder neutron diffraction studies of Cr_2As (*1*, *14*) and Mn_2As (*9*, *12*) have found that they have the orderings shown in Figure 1.5. In Cr_2As, the nearest-neighbor M(I)–M(I) interactions are antiferromagnetically coupled, the M(II)–M(II) interactions ferromagnetically coupled, and the M(I)–M(II) contacts are mixed ferro- and antiferromagnetic coupling. In Mn_2As, the M(I) sheets are internally ferromagnetic, but the nearest-neighbor M(II)–M(II) and M(I)–M(II) interactions are antiferromagnetic. The observed magnetic ordering of CrMnAs has antiferromagnetic M(I)–M(I) coupling, as in Cr_2As, but also antiferromagnetic M(II)–M(II) coupling, as in Mn_2As.

[1] The 1978 paper of Yamaguchi and Watanabe instead showed a ferromagnetic ordering within each M(I) plane (the ordering described as AF9 in section Figure 2.10) (*1*), but Yamaguchi revised that claim in a 1999 paper (*25*).

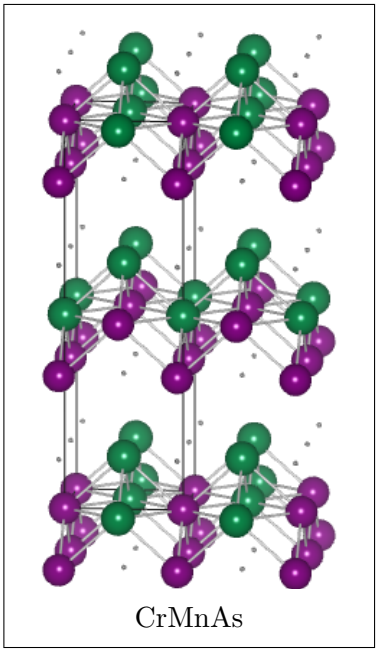

Figure 1.4: The previously observed magnetic structure of CrMnAs (*25*). Purple represents spin-up and green represents spin-down. Grey dots represent arsenic atoms. The magnetic unit cell is outlined in black.

These patterns of magnetic moment for Cr_2As and Mn_2As provide an interesting perspective on the ordering of CrMnAs, according to Fruchart (*21*): He argued that the Cr–Cr (meaning M(I)–M(I)) coupling in CrMnAs is the same as in Cr_2As and the Mn–Mn (M(II)–M(II)) coupling in CrMnAs is the same as in Mn_2As, and that this, in turn, indicates a "very local" range of magnetic interactions. That perspective is suggestive, but with only 88% occupancy of each site, nearly a quarter of the intrasite interactions are not between the predominant atoms, so the picture could be less simple than Fruchart suggests.

Yuzuri reported that the Néel temperature of $Cr_{2.1}As$ was 393 K (*26*); Watanabe found the same Néel temperature with magnetic susceptibility experiments on $Cr_{2.2}As$. Those studies used Cr-rich compounds because stoichiometric Cr_2As tends to decompose at room temperature (*31*), potentially contaminating samples with ferromagnetic Cr_3As_2 (*15*, *26*). Ishimoto et al. measured the magnetic susceptibility versus temperature of powder samples of $Cr_{2.0}As$, $Cr_{2.1}As$, and $Cr_{2.2}As$ and found that all three compounds showed the same magnetic transitions: not only at the Néel temperature of 393 K but also at 175 K (*31*). The transition at 175 K is thought

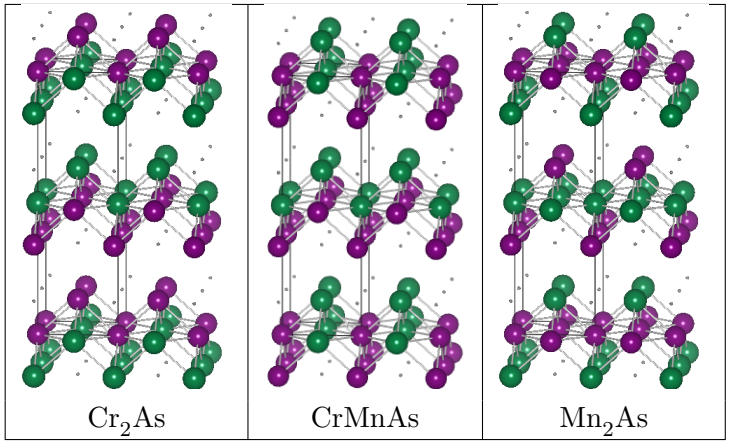

Figure 1.5: The magnetic structures of Cr_2As, CrMnAs, and Mn_2As. These are the magnetic orderings called AF7 and AF3, respectively, in section 2.2. Purple represents spin-up and green represents spin-down. Grey dots represent arsenic atoms. The magnetic unit cells are outlined in black.

to represent an ordering temperature for the M(I) atoms in Cr_2As. The Néel temperature of Mn_2As is about 573 K (*15*, *30*).

1.2 Introduction to the computational methods

1.2.1 VASP

Total energies, magnetic moments, and optimized structures were calculated using VASP, the Vienna Ab-initio Simulation Package, version 4.6, with plane-augmented wave (PAW) pseudopotentials supplied by the creators of the package (*32*). A key challenge for density-functional methods when computing electronic structures is how to treat core electrons; explicitly modeling core electrons requires large numbers of plane waves, which can become computationally unrealistic (*6*). VASP addresses this problem by using pseudopotentials that incorporate the behavior of the valence electrons and the core as a whole (*33*). Several alternatives for defining the functionals are available through VASP. The local-density appromixation (LDA) uses a exchange-correlation functional that depends on charge density, and the local spin-density approximation (LSDA) uses a functional of both charge and spin density (*33*). In the generalized gradient approximation (GGA), the functional also depends on the gradient of those densities (*34*).

A convergence criterion of 10^{-6} eV was used for all VASP calculations reported here. That is, the calculations were stopped when the difference in total energy between consecutive cycles was less than 10^{-6} eV. The maximum kinetic energy for plane-waves to be included in the basis set was also set to 500.00 eV for all calculations here. Keeping those parameters fixed, and using a real-space projection and consistent smearing method, allows results of VASP calculations to be meaningfully compared (*32*).

1.2.2 TB-LMTO-ASA

Band structures, densities of states, and crystal orbital Hamilton population (COHP) curves (*35*) were calculated using the Stuttgart TB-LMTO program, which implements a tight-binding linear muffin-tin orbital (TB-LMTO) algorithm with the atomic spheres approximation (ASA) (*36*, *37*). It describes the core by an atomic-sphere function and separately uses spherical harmonics to explicitly model the valence electrons (*6*, *37*).

1.2.3 Other software tools

The structure pictures included here were prepared with the VESTA 3 software package (*38*). The ICSD's FindIt software package was used to access ICSD data and for generating hypothetical neutron diffraction patterns (*39*).

1.3 Goals

This research is intended to address the following questions:

- Do electronic structure calculations support the experimental finding that CrMnAs has a 12-atom magnetic unit cell with the antiferromagnetic ordering shown in Figure 1.4?
- Can electronic-structure calculations explain why the M(I) site in CrMnAs is preferentially occupied by Cr and the M(II) site is preferentially occupied by Mn?
- Which interatomic interactions play the biggest role in determining the magnetic ordering and coloring of CrMnAs?

CHAPTER 2. RESULTS

2.1 Total energy of six-atom unit cell

The initial phase of this investigation focused on the six-atom chemical unit cell. From prior research, it is known that the magnetic unit cell of CrMnAs is doubled (*21*, *25*), but beginning with the chemical unit cell provided an opportunity to investigate why the magnetic ordering would break the lattice symmetry.

Among the four metal atoms, there are only three possible colorings that would preserve the translational symmetry of the six-atom chemical unit cell: site M(I) entirely occupied by Cr and site M(II) entirely occupied by Mn; equal occupancy of Mn and Cr on both metal sites; and site M(I) entirely occupied by Mn and site M(II) entirely occupied by Cr. Those three colorings are shown in Figure 2.1. For brevity, colorings will be described by the occupation of the M(I) site.

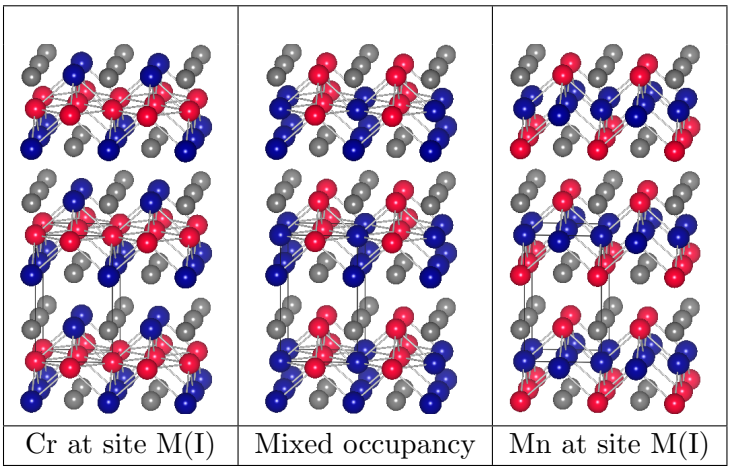

Figure 2.1: Possible colorings of CrMnAs that are unique up to symmetry of the chemical unit cell. Red circles represent chromium, blue represent manganese, and grey represent arsenic. Chemical unit cell is outlined in black.

Similarly, there are five possible magnetic orderings that have a magnetic unit cell equal to the chemical unit cell. The ordering could be ferromagnetic (FM, Figure 2.2a). For the material to be antiferromagnetic while preserving the symmetry of the unit cell, the signs of the atomic moments would have to alternate within each metal site (AFM, Figure 2.2b). If both sites were internally ferromagnetic but with opposite spins, the overall effect would be ferrimagnetic (FiM1, Figure 2.2c). Or one site could be internally ferromagnetic and the other internally antiferromagnetic (FiM2 and FiM3, Figure 2.2d and Figure 2.2e, respectively).

The M(I)–M(I) interactions and M(II)–M(II) interactions in the possible ordering labelled AFM are all antiferromagnetic, and the M(I)–M(II) interactions are mixed ferro- and antiferromagnetically coupled. In all these features, the AFM ordering is similar to the previously observed ordering in CrMnAs (Figure 2.2f) (*25*). The difference between the AFM ordering and the observed ordering of CrMnAs is in the interaction between M(I) sheets along the *c* axis. In the AFM ordering, the M(I) sheets are stacked ferromagnetically; in the observed CrMnAs ordering, the sheets are stacked antiferromagnetically, so the spin of the M(I) atoms alternates in the *c* direction. The distance between M(I) sheets is 6.259 Å, so the through-space interaction between them was expected to be weak, and the total energy of the AFM magnetic ordering was expected to be similar to the total energy of the observed magnetic ordering of CrMnAs.

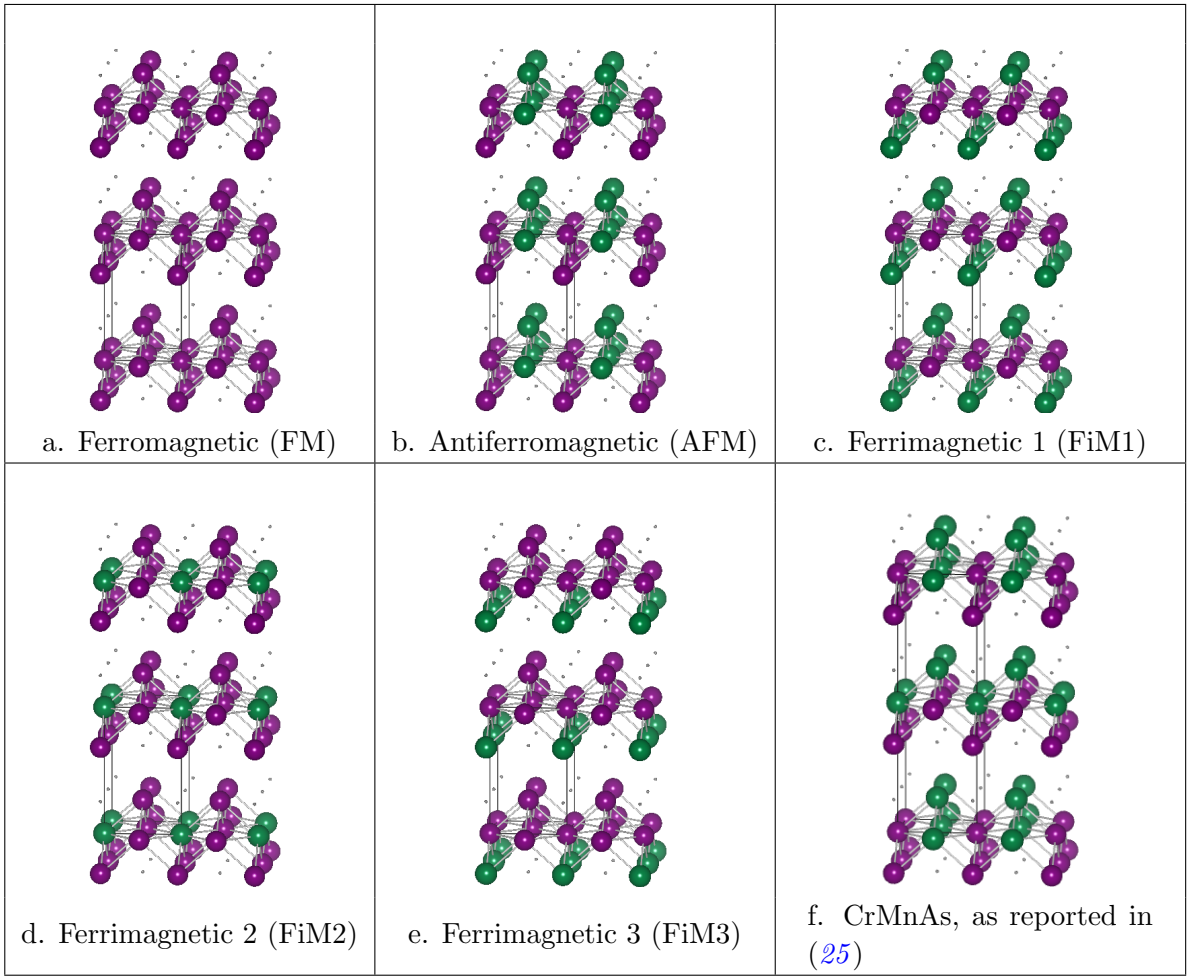

Figure 2.2: (a)–(e) Possible magnetic orderings of CrMnAs that are unique up to symmetry of the chemical unit cell. Purple represents spin-up, and green represents spin-down. As atoms are shown as grey dots. 6-atom chemical unit cell is outlined in black. (f) Experimentally measured ordering of CrMnAs is shown for comparison. 12-atom magnetic unit cell is outlined in black.

2.1.1 Total-energy calculations

Before any magnetic effects were considered, total energies of the six-atom cells were calculated for all three colorings of the chemical unit cell using VASP software. Without spin polarization, the lowest energy coloring was found to be Mn at site M(I) (Table 2.1). Since empirical studies have indicated that the M(I) site is primarily occupied by Cr (*40*), these results indicate that the coloring must be affected by something not captured in the non-spin-polarized six-atom cell, namely larger-scale ordering or magnetic effects.

The two full-occupancy colorings of the six-atom cells were then considered with each of

Table 2.1: Relative total energies of three colorings of non-spin-polarized six-atom cell, calculated by LDA, in meV per formula unit.

Site M(I) occupancy	Excess energy (meV/f.u.)
100% Cr	31.4
50% Cr, 50% Mn	20.0
100% Mn	**0**

the possible magnetic orderings (Table 2.2). For all five magnetic orderings, the LSDA total energy was lower than the LDA total energy; for the lowest-energy magnetic ordering, FiM1 with Mn at M(I), the LSDA total energy was 638.9 meV lower than the LDA total energy for the same coloring. The lowest energy once again belonged to the coloring with 100% of Mn at site M(I). With all three colorings, the lowest energy was with a ferrimagnetic ordering; FiM1 for the Mn-at-M(I) coloring and FiM2 for the Cr-at-M(I) coloring. That FiM1 should have the lowest overall energy is surprising, because it has ferromagnetic intrasite coupling at both metal sites, while the observed magnetic ordering is antiferromagnetic within both sites. The FiM2 coloring does share the antiferromagnetic M(I)–M(I) coupling of the observed ordering, but it has ferromagnetic M(II)–M(II) coupling.

Table 2.2: LSDA relative total energies and net magnetizations of magnetic configurations and colorings of six-atom cell.

	100% Cr at M(I)		**100% Mn at M(I)**	
	Energy (meV/f.u.)	Net magnetization (μ_B)	Energy (meV/f.u.)	Net magnetization (μ_B)
FM	Converged to FiM1		594.6	4.91
AFM	85.8	0	221.2	0
FiM1	160.0	3.17	**0**	0.70
FiM2	132.9	1.75	260.1	2.97
FiM3	147.8	5.79	176.3	3.13

To investigate whether small changes in the geometry of the structure would affect the ground state, the same calculations were repeated but with geometry optimization. In these structural relaxation calculations, VASP was used to find energy minima while varying not just magnetization but also lattice parameters and atomic positions, while maintaining the volume and symmetries of the unit cell (Table 2.3).

Although the exact lattice parameters are not the focus of this study, the magnitude of their variation from empirical values can give some insight into how reasonable these calculations are. In this case, the LDA lattice parameters had the largest deviation from the experimental lattice parameters, with the a parameter 6% smaller and the c parameter 10% larger. Relaxation calculations such as these can serve as a test of the computational model. If the relaxed structures were very different from the experimental structure, it could be an indication that the model was in some way not physically realistic. The fact that the relaxed structures are similar to the input data in this case is reassuring, though not probative. Although varying the geometry introduced some variation in energy, the FiM1 ordering with Mn on site M(I) is still the lowest energy for the six-atom unit cell. With the Cr-at-M(I) coloring, the AFM ordering also remained the lowest with relaxation.

Table 2.3: Relative energies and geometries of magnetic configurations and colorings of six-atom cell with simultaneous optimization of structural parameters. In each entry, first energy (in red) is relative to equivalent calculation without structural relaxation. The second energy (in blue) is relative to lowest-energy of these scenarios with structural relaxation, which was FiM1 with Mn at M(I). μ_{I} and μ_{II} are the magnetic moments per atom at the M(I) and M(II) sites, respectively, in μ_{B}.

Relative to non-relaxed Relative to relaxed FiM1 with Mn at M(I)	**Cr at M(I)**	**Mn at M(I)**
LDA	-74.7 meV/f.u. 740.7 meV/f.u. a = 3.969 Å c = 5.612 Å	-86.2 meV/f.u. 697.9 meV/f.u. a = 3.818 Å c = 6.065 Å
FM	Converged to no moments	-17.5 meV/f.u. 593.6 meV/f.u. a = 3.747 Å c = 6.296 Å $\mu_{\mathrm{I}} = 1.98$ $\mu_{\mathrm{II}} = 0.48$
AFM	-47.5 meV/f.u. 54.8 meV/f.u. a = 3.802 Å c = 6.247 Å $\mu_{\mathrm{I}} = \pm 1.67$ $\mu_{\mathrm{II}} = 3.30$	-55.3 meV/f.u. 182.4 meV/f.u. a = 3.799 Å c = 6.267 Å $\mu_{\mathrm{I}} = \pm 2.01$ $\mu_{\mathrm{II}} = \pm 3.01$
FiM1	-68.1 meV/f.u. 108.4 meV/f.u. a = 3.829 Å c = 6.029 Å $\mu_{\mathrm{I}} = -1.56$ $\mu_{\mathrm{II}} = 3.24$	-16.5 meV/f.u. **0.0 meV/f.u.** a = 3.715 Å c = 6.404 Å $\mu_{\mathrm{I}} = 2.45$ $\mu_{\mathrm{II}} = -2.79$
FiM2	-14.8 meV/f.u.; 149.5 meV/f.u. a = 3.745 Å c = 6.302 Å $\mu_{\mathrm{I}} = 1.36, -2.04$ $\mu_{\mathrm{II}} = 3.29$	Converged to AFM
FiM3	-52.4 meV/f.u.; 96.9 meV/f.u. a = 3.779 Å c = 6.190 Å $\mu_{\mathrm{I}} = 0.99$ $\mu_{\mathrm{II}} = -3.40, 3.30$	-79.1 meV/f.u. 113.7 meV/f.u. a = 3.753 Å c = 6.277 Å $\mu_{\mathrm{I}} = 1.73$ $\mu_{\mathrm{II}} = 2.79, -3.31$

2.1.2 LDA band structure, density of states, and COHP analysis

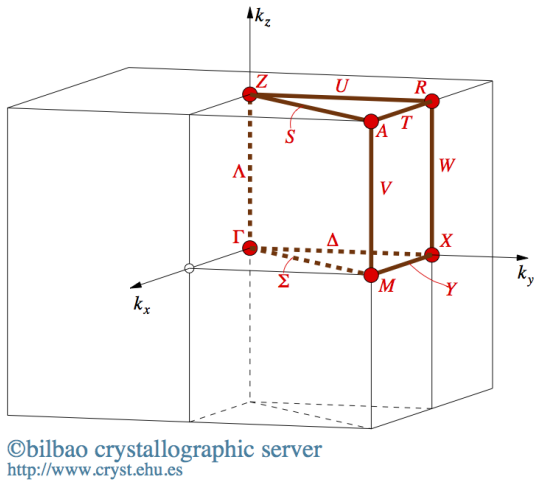

Figure 2.3: Brillouin zone of space group P4/nmm, from Bilbao Crystallographic Server (*41–43*).

The LMTO-ASA software was used to generate band structures for the two full-occupancy colorings of CrMnAs (Figure 2.4 and Figure 2.5). For reference, the Brillouin zone of space group P4/nmm is shown in Figure 2.3 (*41–43*). With Cr at site M(I), the LDA band structure shows a gap at the Fermi energy between A and M (indicated in green on Figure 2.4). This gap represents a low electron density near the Fermi level in those regions of the Brillouin zone, an indication of greater stability in the structure (*44*). In the LDA band structure with Mn at M(I), however, there is a band that crosses the Fermi energy between A and M, providing an indication that the Cr-at-M(I) coloring might be electronically stable (Figure 2.5).

The LDA band structures indicate that neither coloring would be stable without spin polarization, however. The non-spin-polarized band structure for CrMnAs with Cr at site M(I) shows a degeneracy at the Fermi energy near the point X, and another just above the Fermi energy between M and Γ (indicated in red on Figure 2.4). The LDA band structure of CrMnAs with Mn at site M(I) shows similar degeneracies, with one near the Fermi energy at the X point and one slightly above the Fermi energy between M and Γ (indicated in red on Figure 2.5). Such degeneracies at the Fermi energy indicate instabilities that would tend to be resolved by breaking the symmetry of the structure, either through a structural distortion or through spin polarization (*45*, *46*).

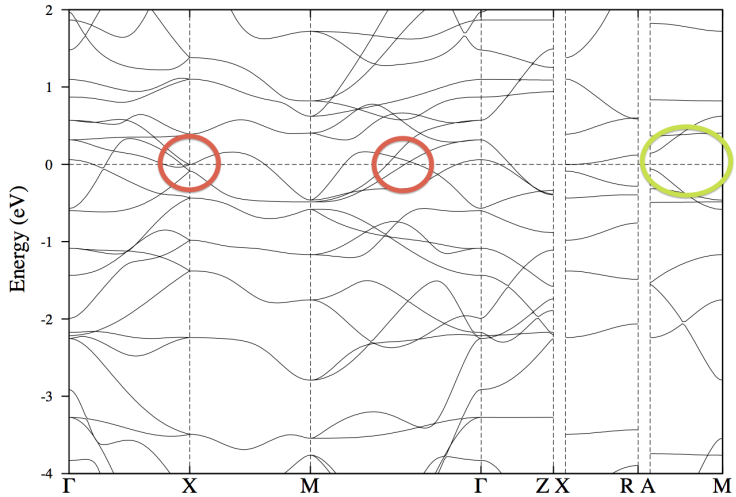

Figure 2.4: LDA band structure for CrMnAs with 100% of Cr at site M(I). Energies are relative to Fermi energy. Red circle shows degeneracies near the Fermi energy. Green circle shows band gap at the Fermi energy.

Table 2.4: Number of bands below Fermi energy at high-symmetry points in Brillouin zone, calculated by LDA for two colorings.

Cr at M(I)						
Point	Γ	X	M	Z	R	A
Bands below ε_F	17	20	20	20	18	20
Electrons below ε_F	34	40	40	40	36	40
Mn at M(I)						
Point	Γ	X	M	Z	R	A
Bands below ε_F	17	20	20	20	18	18
Electrons below ε_F	34	40	40	40	36	36

These band structures are for the chemical unit cell, which contains 36 valence electrons. With both colorings, there are fewer bands below the Fermi energy at the Γ point and more at the higher-wavelength k points at the Brillouin zone boundaries, a reflection of enhanced bonding overlap between the metal d orbitals. The two colorings differ at the A point, with more bands below the Fermi energy for Cr at M(I). Mn is more electronegative than Cr, so the fact that these bands have a lower energy when the more electronegative atom is on site M(II) is another indication that the M(I)–M(I) bonds may play a greater role in determining the coloring than the M(II)–M(II) bonds.

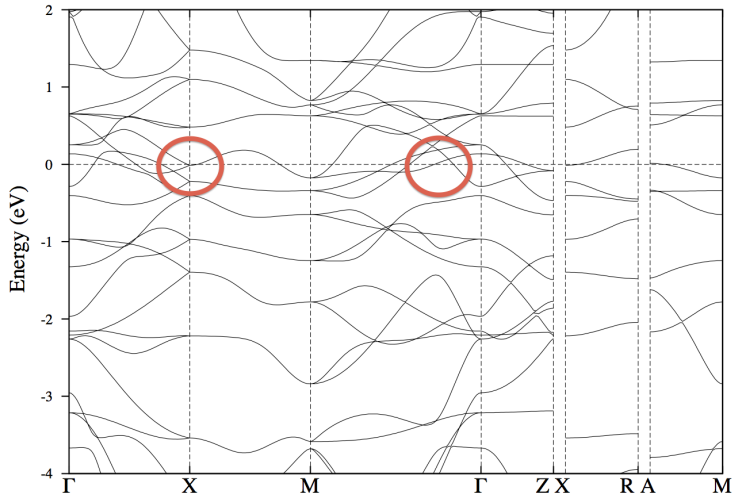

Figure 2.5: LDA band structure for CrMnAs with 100% of Mn at site M(I). Energies are relative to Fermi energy. Red circles show the degeneracy at the Fermi energy at Γ.

The non-spin-polarized (LDA) density of states (DOS) was calculated using the LMTO-ASA package. Overall DOS curves for the two full-occupancy colorings of CrMnAs are shown in Figure 2.6. With both colorings, the Fermi energy lies near a peak in the total DOS; the peak is slightly above the Fermi level with Cr at M(I) and slightly below the Fermi level with Mn at M(I). A breakdown of the atomic contributions to each DOS shows that, in both cases, the M(II) metal is the source of that peak Figure 2.7. Peaks in the DOS curve at the Fermi level are generally indicative of electronic instability that may be resolved by either a spin polarization or a structure distortion, with the type of magnetic ordering related to the nature of the orbital interactions in the material (*3*, *4*, *12*).

In order to examine the nature of particular nearest-neighbor interactions, crystal orbital Hamiltonian population (COHP) curves were generated for these two full-occupancy colorings of CrMnAs. COHP analysis is a method for attributing the band-structure energy of a compound to particular orbital interactions (*35*, *46*). Positive COHP values indicate an antibonding interaction, and negative COHP values indicate a bonding interaction. In order to facilitate interpretation, and to preserve the analogy to crystal orbital overlap population (COOP) analysis, results are usually presented in graphs of –COHP, rather than COHP (*3*).

Non-spin-polarized COHP curves with Cr at M(I) and with Mn at M(I) are shown in Figure 2.8 and Figure 2.9, respectively. For both colorings, the M(I)–M(I) interaction is slightly

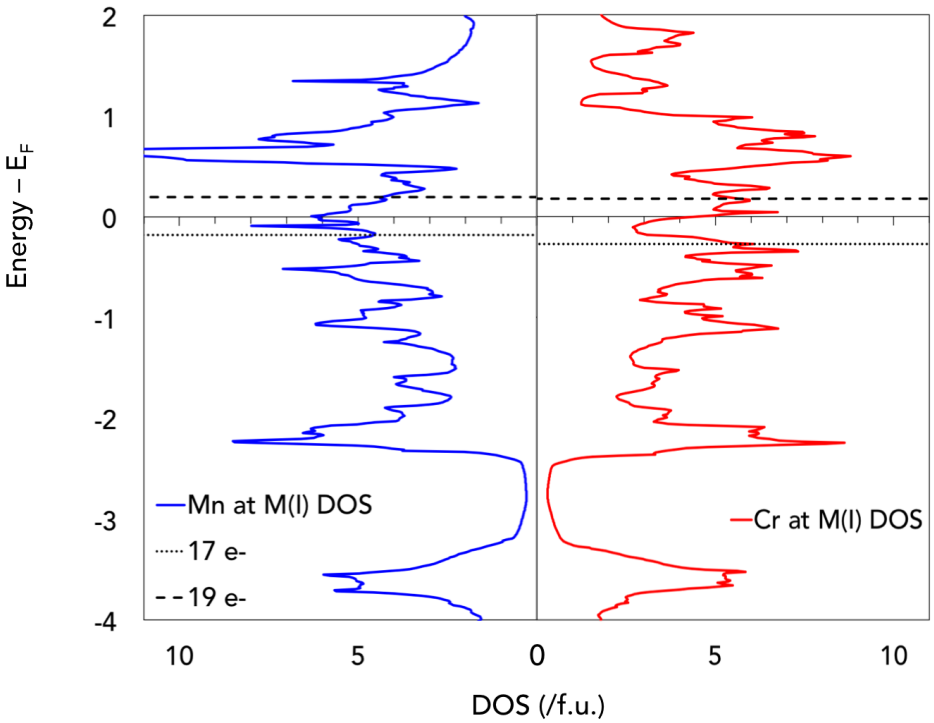

Figure 2.6: Non-spin-polarized densities of states for CrMnAs with two colorings.

antibonding at the Fermi level and the M(I)–M(II) interaction is also antibonding with similar magnitude. Both the M(I)–M(I) and M(I)–M(II) interactions are more strongly antibonding with Mn at M(I) than with Cr at M(I). The M(II)–M(II) interaction is antibonding with the Cr-at-M(I) coloring but nonbonding with the Mn-at-M(I) coloring. The metal–As interactions are both slightly bonding with Cr at M(I), but the M(I)–As interaction is nonbonding with Mn at M(I).

Cr_2As, CrMnAs, and Mn_2As have 17, 18, and 19 valence electrons per formula unit, respectively. The Fermi levels that are equivalent to valence electron counts of 17 and 19 are indicated on Figure 2.8 and Figure 2.9. With Cr at M(I), the 17-electron energy level falls at a bonding peak in the M(I)–M(I) COHP curve. The M(I)–M(II) and M(II)–M(II) remain nonbonding at the 17-electron energy level. With Mn at M(I), the M(I)–M(I) and M(I)–M(II) interactions remain antibonding at the 19-electron energy level, and the M(II)–M(II) interaction remains nonbonding.

Integrating –COHP over energy produces an integrated COHP (ICOHP) value, which in-

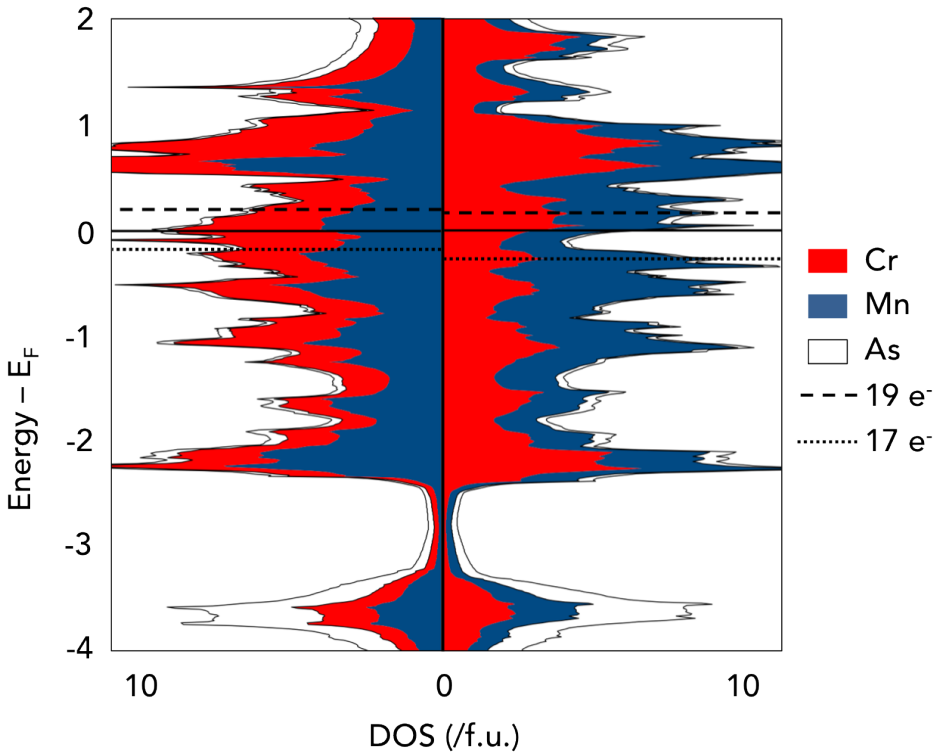

Figure 2.7: Partial densities of states for CrMnAs with 100% of Mn at M(I) (left) and 100% of Cr at M(I) (right).

dicates the order of covalent bond strength (*47*, *48*). Multiplying the ICOHP for each bond type by the number of such bonds gives the ICOHP per formula unit, listed in Table 2.5. The metal–As interactions have the highest –ICOHP, indicating strong orbital interactions. Adding the ICOHPs for the significant bond types gives an energy-weighted covalency index. Although the LDA total energy was lower with Mn at M(I) than with Cr at M(I) (Table 2.1, the more negative ICOHP with Cr at M(I) indicates that the bond energies may favor that coloring (*49*).

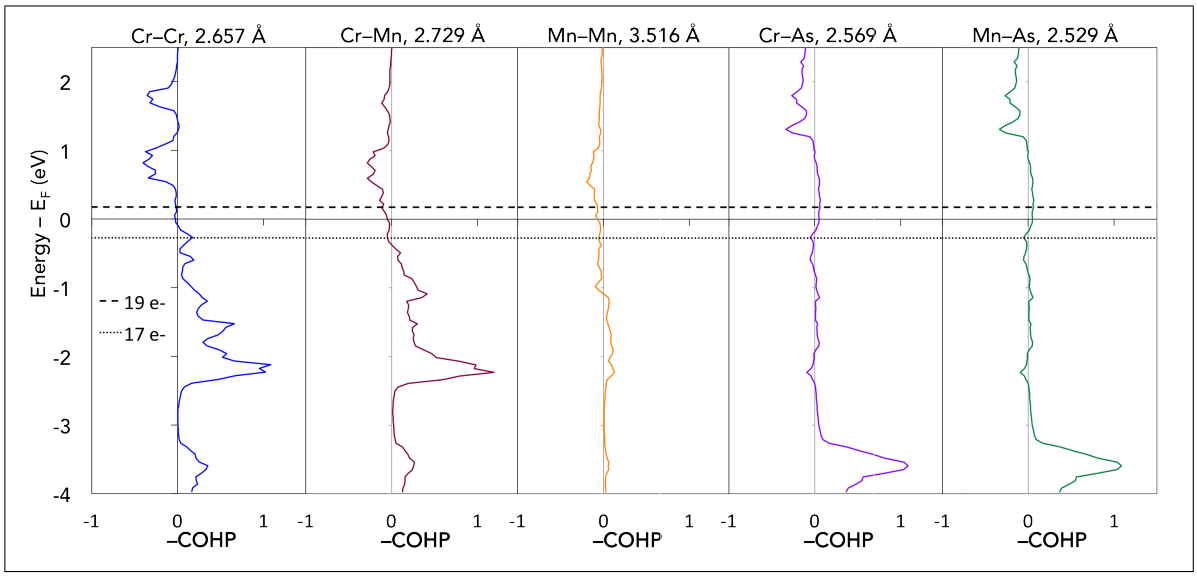

Figure 2.8: Non-spin-polarized COHP curves for CrMnAs with 100% of Cr at site M(I)

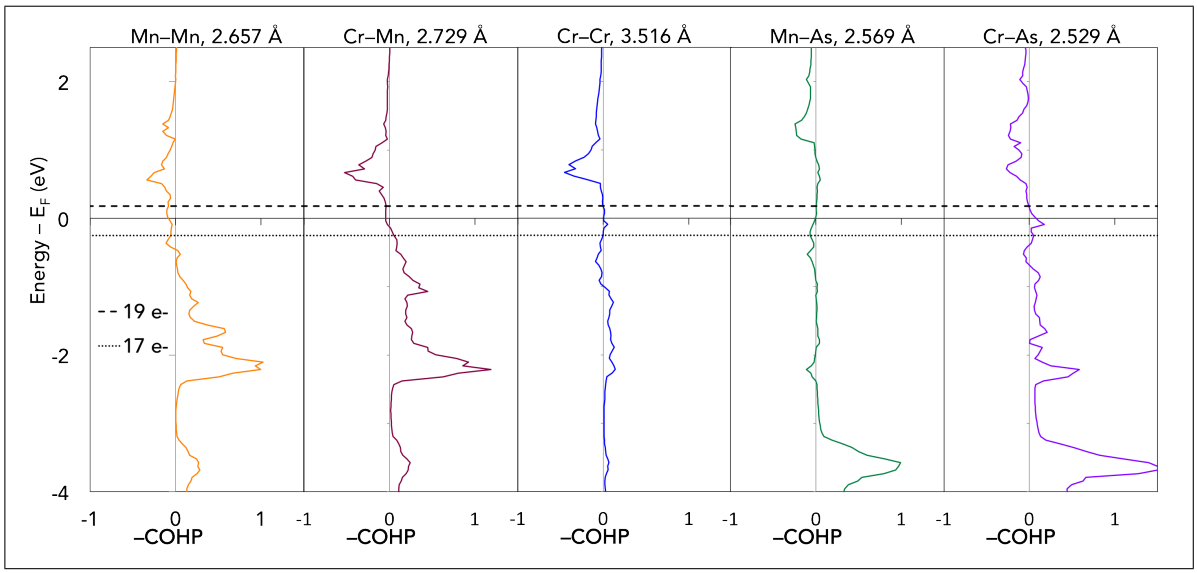

Figure 2.9: Non-spin-polarized COHP curves for CrMnAs with 100% of Mn at site M(I)

Table 2.5: –ICOHP values, in eV per formula unit, for two colorings of CrMnAs without spin polarization.

		Cr at M(I)	**Mn at M(I)**
Bond type	Length (Å)	–ICOHP (eV/f.u.)	–ICOHP (eV/f.u.)
M(I)–M(I)	2.657	2.61	2.25
	3.758	0.13	0.10
M(I)–M(II)	2.729	4.75	4.69
M(II)–M(II)	3.516	0.51	0.58
	3.758	0.09	0.13
M(I)–As	2.569	6.73	6.43
M(II)–As	2.529	2.58	2.63
	2.667	6.77	6.94
Total		**24.18**	**23.76**

2.2 Total energy of 12-atom supercell

Diffraction studies have concluded that the magnetic unit cell of CrMnAs is doubled along the c direction from the chemical unit cell (*20*), so the results from the six-atom cell were used to guide similar investigation of a 12-atom cell. Expanding from four to eight metal atoms sharply increases the combinatorial possibilities for both colorings and magnetic orderings. Given that there is no reason to suspect that partial-occupancy colorings would have any definite pattern that would be captured by this particular supercell, it would not be particularly instructive to perform calculations for all of those possibilities. Instead, this portion of the investigation focused on the two possible full-occupancy colorings.

Because empirical studies have consistently identified antiferromagnetic ordering in CrMnAs, as well as Cr_2As and Mn_2As, and the six-atom cell results also supported the assumption of antiferromagnetism, the 12-atom calculations are limited to 10 possible antiferromagnetic cases. Those cases were found by Zhang to be most instructive in the Cr_2As and Mn_2As systems (*22*). These antiferromagnetic cases are labeled as shown in Figure 2.10.

The calculations on the chemical unit cell provided indications that the M(I)–M(I) and M(I)–M(II) interactions are perhaps most influential in determining the antiferromagnetism of CrMnAs, so these 10 magnetic orderings can be grouped according to the nature of those interactions. AF1, AF2, and AF10 all have the same M(I) spin configuration as AF3, the ordering seen in Mn_2As (*15*, *26*): each M(I) slab is internally ferromagnetic, with the spin direction alternating between slabs. The M(I) slabs are internally antiferromagnetic in AF4, AF5, AF6, AF7 (the ordering reported in Cr_2As (*1*)), and AF8 (the ordering reported in CrMnAs (*25*)). The M(I)–M(II) interactions can be divided into four categories. Each M(I) atom has four nearest-neighbor M(II) atoms. In AF1, AF2, AF4, AF5, and AF7, each M(I) atom has two nearest neighbors with the same spin as it and two with the opposite spin. In AF6, AF8, and AF9, half of the M(I) atoms are coupled ferromagnetically with all four nearest-neighbor M(II) atoms and half are coupled antiferromagnetically with the nearest-neighbor M(II) atoms. In AF3, every M(I) atom is coupled antiferromagnetically with its nearest M(II)

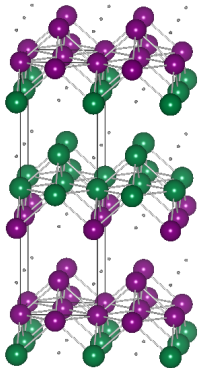 AF1	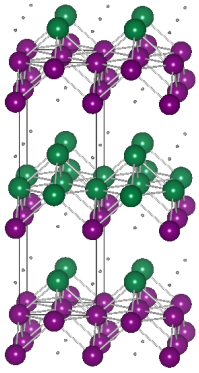 AF2	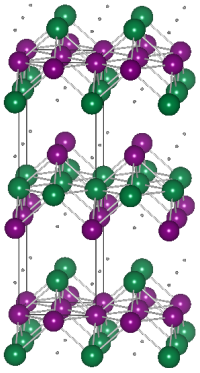 AF3 Reported ordering of Mn_2As (*15*, *26*)	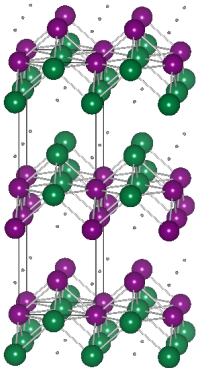 AF4	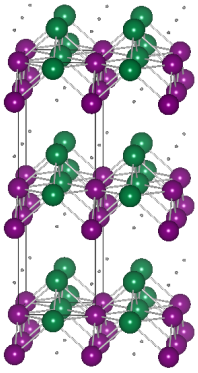 AF5
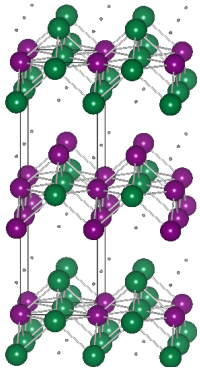 AF6	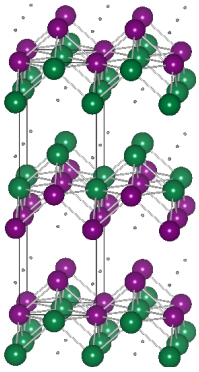 AF7 Reported ordering of Cr_2As (*1*)	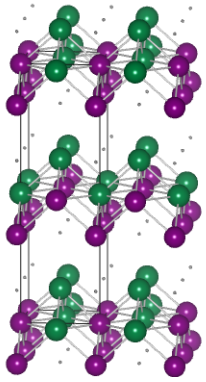 AF8 Reported ordering of CrMnAs (*25*)	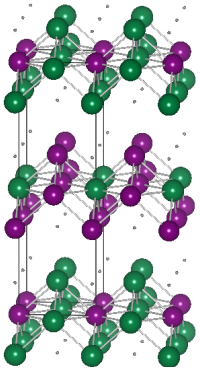 AF9	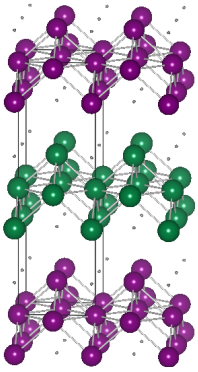 AF10

Figure 2.10: The 10 symmetrically unique antiferromagnetic orderings of 12-atom supercell considered here. Purple represents spin up and green represents spin down. Arsenic atoms are indicated by a black dot.

neighbors, and, in AF10, every M(I) atom coupled ferromagnetically with its nearest M(II) neighbors.

Total energies for those 10 antiferromagnetic orderings and two colorings were calculated using VASP. The results are shown in Table 2.6 and displayed graphically in Figure 2.11. The calculated moments on each metal site are shown in Table 2.7. The AF3 ordering with Mn at M(I) has the lowest energy per formula unit of any of the 12-atom-cell scenarios, and it is also 74.6 meV per formula unit lower than the lowest-energy of the 6-atom cases, FiM1 with Mn at M(I).

If the Cr-at-M(I) coloring is assumed, the AF4 and AF7 orderings have the lowest energies, differing by only 0.4 meV. AF8, the ordering suggested by experiment, is 13 meV higher in energy per formula unit than AF4 and AF7. Within the AF8 ordering, however, the Cr-at-M(I) coloring is preferred by 153 meV. In fact, the Cr-at-M(I) coloring is preferred with every magnetic ordering except the 12-atom AF3 case, the 6-atom FiM1 case, the nonmagnetic (LDA) case, and the three cases (AF1, AF10, and FM) that failed to converge with Cr at M(I).

Table 2.6: Calculated total energies for given different magnetic orderings and two colorings. All calculations assume geometric parameters as shown in Table 1.3, doubled along the c axis for larger-supercell orderings. Energies are in meV/f.u., relative to lowest-energy case, which is AF3 with Mn at M(I).

	Cr at M(I)	**Mn at M(I)**
AF1	Converged to AF7	304.4
AF2	192.6	239.8
AF3	176.8	**0**
AF4	154.2	364.9
AF5	160.4	295.8
AF6	187.8	273.1
AF7	154.6	362.5
AF8	167.8	320.5
AF9	198.1	309.6
AF10	Converged to AF3	495.5
AFM	160.4	295.8
FiM1	234.7	74.6
FiM2	207.5	334.8
FiM3	222.5	250.9
FM	Converged to FiM1	669.3
LDA	873.6	842.2

Table 2.7: Average magnitude of magnetic moments on each metal atom given different antiferromagnetic orderings of 12-atom supercell. Corresponding total energy results are in Table 2.6.

	Cr at M(I)		Mn at M(I)	
	M(I)	**M(II)**	**M(I)**	**M(II)**
AF1	*	*	1.94	2.50
AF2	0.90	3.24	1.96	2.81
AF3	1.66	3.19	2.42	2.86
AF4	1.39	3.23	1.83	2.58
AF5	1.64	3.22	2.08	2.80
AF6	1.84	3.23	1.90	2.76
AF7	1.42	3.21	1.92	2.54
AF8	1.53	3.23	1.97	2.81
AF9	1.80	3.22	1.97	2.74
AF10	*	*	2.29	3.06

* Converged to different ordering

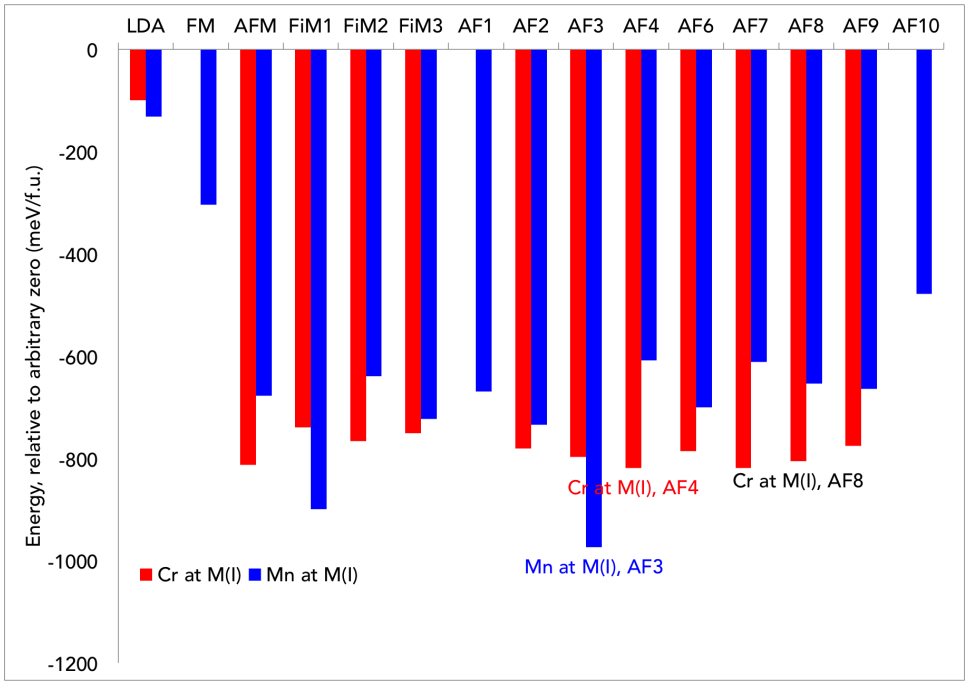

Figure 2.11: LDA and LSDA total energies of two colorings and 15 magnetic orderings. For convenience, energy zero is set at 100 meV/f.u. above LDA energy with Cr at M(I). The lack of red bars for FM, AF1, and AF10 indicate that those orderings converged to different magnetic orderings. FM converged to FiM1, AF1 converged to AF7, and AF10 converged to AF3.

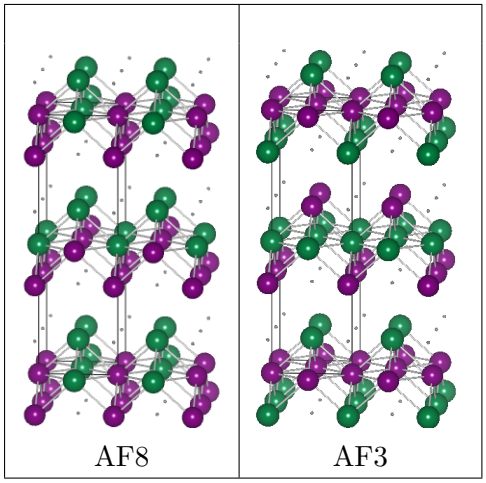

Figure 2.12: Left: AF8, the previously observed magnetic ordering of CrMnAs. Right: AF3, the magnetic ordering with the lowest calculated energy. Purple represents spin-up and green represents spin-down. Grey dots represent arsenic atoms. Magnetic unit cell is outlined in black.

To see whether the outcome of the calculations was sensitive to the geometric parameters, the VASP calculations for AF3 and AF8 orderings were repeated with structural relaxation, optimizing the lattice parameters and atom positions. Results of those calculations are given in Table 2.8 and Table 2.9. As with the calculations without relaxation, the Mn-at-M(I) coloring was preferred for AF3, and the Cr-at-M(I) coloring was preferred for AF8. Unlike in the earlier results, the AF3 ordering had a lower energy with Cr at M(I) than the AF8 ordering with Cr at M(I). Because they represent ground states with respect to different geometries, these results are not directly comparable, but they suggest some parameter sensitivity to magnetic ordering.

To further clarify the significance of the structural parameters, LSDA total energies of the AF3 and AF8 cases with both colorings were calculated using the geometries that resulted from structural relaxation on the AF3 ordering with Mn at M(I) and on the AF8 ordering with Cr at M(I). The results, shown in Table 2.10, follow the same pattern as they did when using the structural parameters from the literature: The lowest-energy case is AF3 ordering with Mn at M(I), but the AF8 ordering is preferred over AF3 when Cr-at-M(I) coloring is assumed.

Figure 2.12 shows the experimentally observed ordering, AF8, and the calculated low-energy ordering, AF3, side-by-side. The M(II) metals are ordered antiferromagnetically in both cases, but the M(I) metals are ordered antiferromagnetically in AF8 and ferromagnetically in AF3.

Table 2.8: Structural relaxation results for AF3 magnetic ordering with two full-occupany colorings. Energy is relative to value without optimization (Table 2.6).

Magnetic ordering:	AF3			
Coloring:	Cr at M(I)			
Energy:	−69.6 meV relative to AF3, Cr at M(I), without relaxation			
	122.6 meV relative to lowest-energy relaxed case (AF3, Mn at M(I))			
Lattice parameters:	$a = 3.845$ Å			
	$c = 5.980$ Å			
	Atom	x	y	z
	M(I)	0	0	0
	M(I)	0.5	0.5	0
Atom locations:	M(II)	0	0.5	0.309
	M(II)	0.5	0	0.691
	As	0	0.5	0.731
	As	0.5	0	0.269
Magnetic ordering:	AF3			
Coloring:	Mn at M(I)			
Energy:	−15.4 meV relative to AF3, Cr at M(I), without relaxation			
	Lowest-energy relaxed case			
Lattice parameters:	$a = 3.723$ Å			
	$c = 6.378$ Å			
	Atom	x	y	z
	M(I)	0	0	0
	M(I)	0.5	0.5	0
Atom locations:	M(II)	0	0.5	0.326
	M(II)	0.5	0	0.674
	As	0	0.5	0.724
	As	0.5	0	0.276

As discussed above, all of the nearest-neighbor M(I)–M(II) interactions are antiferromagnetic in AF3, but half are ferromagnetic in AF8. The nearest-neighbor M(I)–M(I) interactions are also different, entirely ferromagnetic in AF3 and entirely antiferromagnetic in AF8. Where AF3 and AF8 are similar is in the M(II)–M(II) interactions, which are entirely antiferromagnetic in both cases.

Grouping the other LSDA total-energy results according to the type of coupling in the M(I)–M(I) bonds, a pattern emerges. Seven of the magnetic orderings have antiferromagnetic coupling between the M(I) atoms, and the Cr-at-M(I) coloring is preferred in all seven cases. Of the seven orderings that have ferromagnetic M(I)–M(I) coupling, the Mn-at-M(I) coloring

Table 2.9: Structural relaxation results for AF8 magnetic ordering with two full-occupany colorings. Values are for chemical unit cell. Energy is relative to value without optimization (Table 2.6).

Magnetic ordering:	AF8			
Coloring:	Cr at M(I)			
Energy:	−43.4 meV relative to AF8, Cr at M(I), without relaxation			
	139.8 meV relative to lowest-energy relaxed case (AF3, Mn at M(I))			
Lattice parameters:	$a = 3.772$ Å			
	$c = 6.214$ Å			
	Atom	x	y	z
	M(I)	0	0	0
	M(I)	0.5	0.5	0
Atom locations:	M(II)	0	0.5	0.330
	M(II)	0.5	0	0.670
	As	0	0.5	0.734
	As	0.5	0	0.266
Magnetic ordering:	AF8			
Coloring:	Mn at M(I)			
Energy:	−54.6 meV relative to AF8, Mn at M(I), without relaxation			
	281.3 meV relative to lowest-energy relaxed case (AF3, Mn at M(I))			
Lattice parameters:	$a = 3.766$ Å			
	$c = 6.235$ Å			
	Atom	x	y	z
	M(I)	0	0	0
	M(I)	0.5	0.5	0
Atom locations:	M(II)	0	0.5	0.327
	M(II)	0.5	0	0.673
	As	0	0.5	0.737
	As	0.5	0	0.263

is preferred in all but two cases. In those two cases, the energy difference between the colorings is not huge; the Cr-at-M(I) coloring is preferred by 28.4 meV/f.u. for FiM3 and by 47.2 meV for AF2.

These LSDA results are consistent with the LDA COHP curves shown in Figure 2.8 and Figure 2.9. A zero or "nonbonding" value of the LDA –COHP at the Fermi energy is an indicator of an instability that could be resolved by antiferromagnetic ordering, and a negative, or "antibonding" –COHP at the Fermi energy indicates an instability that could be resolved by ferromagnetic ordering. With Cr at M(I), the LDA COHP curves were nonbonding for M(I)–M(I), nonbonding for M(I)–M(II), and antibonding for M(II)–M(II), indicating that

Table 2.10: LSDA total energies for AF3 and AF8 magnetic orderings and two colorings, without relaxation, using geometry resulting from earlier relaxation calculations. Energies are in meV/f.u., relative to lowest-energy case with same geometry.

With structural parameters from AF3 relaxation calculation with Mn at M(I) (Table 2.8)		
	Cr at M(I)	**Mn at M(I)**
AF3	140.9	**0**
AF8	106.8	252.7
With structural parameters from AF8 relaxation calculation with Cr at M(I) (Table 2.9)		
	Cr at M(I)	**Mn at M(I)**
AF3	222.4	**0**
AF8	172.9	281.3

those bonds would be antiferromagnetic, antiferromagnetic, and ferromagnetic, respectively. Only the AF4 and AF7 orderings have those types of coupling, and AF4 and AF7 were the lowest-energy orderings with the Cr-at-M(I) coloring. Similarly, the LDA COHP curves with Mn at M(I) were antibonding for M(I)–M(I), nonbonding for M(I)–M(II), and nonbonding for M(II)–M(II), indicating ferromagnetic, antiferromagnetic and antiferromagnetic coupling, respectively. Those types of coupling are present only in AF3, which was preferred with the Mn-at-M(I) coloring.

CHAPTER 3. CONCLUSION

The electronic-structure calculations described here do strongly agree with the experimental finding that spin polarization will occur in CrMnAs. The band structures shown in Figure 2.4 and Figure 2.5 show degeneracies at the Fermi energy for either coloring of CrMnAs; those degeneracies could be resolved by either spin polarization or structural distortions. The metal–metal LDA COHP curves are nonbonding or antibonding at the Fermi energy for both colorings, which has been found in other compounds to suggest that spin polarization will occur (*4*).

The calculations do not so far agree with empirical results about what magnetic ordering will result from spin polarization. Powder neutron diffraction studies of CrMnAs have found the magnetic ordering to be AF8, with antiferromagnetic coupling within each metal site and mixed ferro-/antiferromagnetic coupling between the metal sites (*25*). Instead, when either coloring of the metal atoms was allowed, the magnetic ordering with the lowest total energy was calculated to be AF3, the magnetic ordering that has been observed in Mn_2As (*30*, *50*), which has ferromagnetic M(I)–M(I) coupling. When the Cr-at-M(I) coloring was required, the AF8 ordering was one of four lower-energy orderings, all of which share antiferromagnetic M(I)–M(I) coupling. A similar result has been obtained by Zhang for the binary arsenides; LSDA calculations found that the same four magnetic orderings had the lowest energies in Cr_2As and Mn_2As (*12*).

The LDA COHP curves indicate the type of magnetic coupling likely to arise in each metal–metal bond. Among the orderings considered, the COHP curves suggest that with Cr at M(I), the magnetic ordering would be AF4 or AF7, and with Mn at M(I), the magnetic ordering would be AF3. The fact that the LDA COHP curves, which were calculated with LMTO-ASA, suggest the same result as the LSDA total-energy calculations, which were performed with VASP, suggests that the calculated ground state is not an artifact of a particular program. Instead,

the fact that the calculated ground state did not match the observed magnetic ordering may indicate that the magnetic ordering does not have the symmetry assumed here, of the chemical unit cell doubled along the c axis; that the magnetic ordering is sensitive to the coloring in a way not captured by only considering full-occupancy colorings; or that the slight excess of Cr in the experimental samples affects the magnetic ordering, as discussed below. In order to address the former two possibilities, scenarios with the unit cell expanded along the a and b axes will be modeled, with both longer-scale magnetic orderings and partial-occupancy colorings.

A major motivation for the choice of CrMnAs was the expected predictive power of valence electron count; because Cr_2As, CrMnAs, and Mn_2As have 17, 18, and 19 valence electrons, respectively, it was hoped that the $(Cr_xMn_{1\text{-}x})_2As$ series could suggest heuristics by which valence electron count could be used to predict structure and mechanical properties based on composition. The calculations included here all assumed a stoichiometric composition of CrMnAs, which would have exactly 18 valence electrons. The empirical studies referenced, however, have used Cr-rich $Cr_{1+\epsilon}MnAs$, which means that the measured samples would have had a slightly lower valence electron count than stoichiometric CrMnAs. An important future direction will be to examine the possibility that the ground state could be dependent on such small changes in composition. The spin-polarized density of states will be calculated for each possible magnetic ordering of stoichiometric CrMnAs. Each LSDA DOS will be numerically integrated as a function of valence electron count in the neighborhood of the Fermi level. It is hoped that will indicate whether small changes in the valence electron count can change which ground state is predicted by the calculations. That method has previously been successful in predicting the ground state in $Ti_{9-n}Fe_{2+n}Ru_{18}B_8$ compounds (*6*).

Both the LDA and LSDA total-energy calculations found a lowest energy with Mn at M(I), contrary to the experimental observation that site M(I) is occupied 88% by Cr and 12% by Mn (*2*). It was found, however, the magnetic ordering was assumed to be as observed, then the Cr-at-M(I) coloring was preferred. The LDA calculations provided other suggestions of stability for the Cr-at-M(I) coloring as well. There is a band gap at the Fermi energy between points M and A in the Cr-at-M(I) coloring that does not exist in the Mn-at-M(I) coloring (Figure 2.4 and Figure 2.5). The Fermi energy falls near a pseudogap in the LDA density of

states with Cr at M(I), though not with Mn at M(I) (Figure 2.6). That pseudogap lies slightly below the stoichiometric CrMnAs Fermi energy, which is the direction that the Fermi energy would be shifted if excess Cr were a factor in the coloring. Finally, the total –ICOHP is higher with Cr at M(I) than with Mn at M(I), indicating a greater overlap population in the former case (Table 2.5). None of these factors overrides the total-energy results in determining the coloring of CrMnAs, but each is an indication of a possible source of stability for the Cr-at-M(I) coloring.

It is possible that the true ground state of CrMnAs is not the reported AF8 ordering for reasons other than stoichiometry. The magnetic moments might be disordered or have longer-range ordering than is captured in the 12-atom unit cell, and there might be more than one magnetic phase present. To examine the likelihood of a mixed magnetic phase being present in the experimental samples, a simple probability calculation can be applied to a set of possible states at a given temperature, assuming a Boltzmann distribution of those states. Preliminary results of those calculations, taking into account only the antiferromagnetic orderings considered here, suggests that a mix of phases could be present for the Cr-at-M(I) coloring at the experimental annealing temperature, 1173 K. The low-temperature transition at 230 K, which has been assumed to be the ordering temperature of site M(I), could also be an indication of a more complicated picture. The COHP method does not take into account the possibility of indirect exchange, where moments are coupled by way of an intermediary, so exchange parameters will be calculated to determine how significant indirect exchange is in CrMnAs.

Another direction for future work will be to repeat the total energy calculations with the inclusion of an empirical orbital repulsion corrections (LSDA+U). The previous study on M_2As considered the effect of various Hubbard-type U parameters on the predicted ground state of Mn_2As. While the empirically observed ground state was predicted by LSDA without the correction, small changes in the U parameter were found to change the predicted ground state. The expected antiferromagnetic ground state was predicted with $U = 0$ and $U > 2$ eV, but a ferrimagnetic ground state was predicted when $0.5 \text{ eV} \leq U \leq 2 \text{ eV}$ (*12*).

Moving forward from tetragonal CrMnAs, this research project will look at hexagonal forms of the 3d-metal arsenides. $Cr_{0.55}Mn_{0.45}As$ has been observed in a hexagonal structure, and

CrFeAs is known only in a hexagonal structure . The computational techniques used here will be applied to the hexagonal systems, and the origins of the transition between the systems will be examined. The focus will be on whether it is possible to use valence electron count as a proxy for stoichiometry across structural types. The lessons learned on the 3d-metal arsenide project will also be applied to more boride systems with much larger unit cells. Previous work by Fokwa et al. has focused on some of the novel structural and magnetic properties of intermetallic borides featuring 3*d* transition metals, including triangular subunits in $Ti_{0.33}Cr_{1.67}Ir_2B_2$ (*51*). That research will be extended by examining that and other intermetallic borides, with the goal of gaining insights that can be used to direct or explain that synthetic research.

BIBLIOGRAPHY

[1] Yamaguchi, Y.; Watanabe, H. Magnetic Properties of $(CrMn)_2As$ System. *J. Phys. Soc. Jpn.* **1978**, *44*, 1782–1786.

[2] Fruchart, D. Structural and Magnetic Investigations of Some Transition Metal Arsenides. *Proceedings of the VII International Conference on Solid Compounds of Transition Elements*, Grenoble, France, 1982; p IIIA1.

[3] Landrum, G.; Dronskowski, R. The Orbital Origins of Magnetism: From Atoms to Molecules to Ferromagnetic Alloys. *Angew. Chem., Int. Ed.* **2000**, *39*, 1560–1585.

[4] Dronskowski, R.; Korczak, K.; Lueken, H.; Jung, W. Chemically Tuning between Ferromagnetism and Antiferromagnetism By Combining Theory and Synthesis in Iron/Manganese Rhodium Borides. *Angew. Chem., Int. Ed.* **2002**, *41*, 2528–2532.

[5] Fokwa, B. P. T.; Lueken, H.; Dronskowski, R. Rational Synthetic Tuning between Itinerant Antiferromagnetism and Ferromagnetism in the Complex Boride Series $Sc_2FeRu_{5-n}Rh_nB_2$ $(0 \leq n \leq 5)$. *Chem.—A European Journal* **2007**, *13*, 6040–6046.

[6] Brgoch, J. Ph.D. thesis, Iowa State University: Ames, Iowa, 2012.

[7] Hurd, C. M. Varieties of magnetic order in solids. *Contemporary Physics* **1982**, *23*, 469–493.

[8] Ko, H. Ph.D. thesis, Iowa State University: Ames, Iowa, 2008.

[9] Shirakawa, K.; Ido, H. Magnetic Transition of the Mn_2Sb-Mn2As System. *J. Phys. Soc. Jpn.* **1976**, *40*, 666–673.

[10] Chonan, T.; Yamada, A.; Motizuki, K. Electronic Band Structures of Cu_2Sb-Type Intermetallic Compounds. *J. Phys. Soc. Jpn.* **1991**, *60*, 1638–1646.

[11] Katsuraki, H.; Achiwa, N. The Magnetic Structure of Fe_2As. *J. Phys. Soc. Jpn.* **1966**, *21*, 2238–2243.

[12] Zhang, Y.; Brgoch, J.; Miller, G. J. Magnetic Ordering in Tetragonal 3d Metal Arsenides M_2As (M = Cr, Mn, Fe): An Ab Initio Investigation. *Inorg. Chem.* **2013**.

[13] Jain, S.; Das, A.; Srivastava, B.; Krishnamurthy, A.; Paranjpe, S. Magnetic Behaviour of $(Fe_{0.85}Cr_{0.15})_2As$. *Pramana* **2004**, *63*, 207–212.

[14] Yamaguchi, Y.; Watanabe, H.; Yamauchi, H. Neutron diffraction study of Cr_2As. *J. Phys. Soc. Jpn.* **1972**.

[15] Watanabe, H.; Nakagawa, Y.; Sato, K. On the Neutron Diffraction Study of Cr_2As. *J. Phys. Soc. Jpn.* **1965**, *20*, 2244–2248.

[16] Selte, K.; Kjekshus, A.; Andresen, A. Magnetic Structures and Properties of $Mn_{1\text{-}t}Fe_tAs$ Phases. *Acta Chem. Scand., Ser. A* **1974**, *28*, 61–70.

[17] Yoshii, S.; Katsuraki, H. Crystal Structure and Magnetic Property of FeMnAs. *J. Phys. Soc. Jpn.* **1966**, *21*, 205–&.

[18] Yoshii, S.; Katsuraki, H. Neutron Diffraction Study of FeMnAs. *J. Phys. Soc. Jpn.* **1967**, *22*, 674–&.

[19] Miller, G. J. The "Coloring Problem" in Solids: How It Affects Structure, Composition and Properties. *Eur. J. Inorg. Chem.* **1998**, *1998*, 523–536.

[20] Ohoyama, K.; Kanouchi, T.; Nemoto, K.; Ohashi, M.; Kajitani, T.; Yamaguchi, Y. HERMES, the High-Efficiency Multipurpose Powder Diffractometer. *Phys. B (Amsterdam, Neth.)* **1998**, *241-243*, 213–215.

[21] Fruchart, D. Magnetic couplings in MM′X compounds of Cu_2Sb type of structure (M, M′ = d-metals, X= p-elements as P, As, Sb, ...). *Solid State Sci.* **2005**, *7*, 767–775.

[22] Zhang, Y. *Magnetic Properties of M_2As (M=Cr, Mn, Fe)*, Presentation in Miller/Corbett group meeting, Iowa State University, Ames, Iowa, 2011.

[23] Hollan, L. Étude Structurale et Magnétique d'Arséniures Mixtes M_2As. *Annales de Chimie* **1966**, 437–448.

[24] Zhang, Y. Personal conversation, April 2013.

[25] Yamaguchi, Y.; Ohoyama, K.; Kanouchi, T.; Ohashi, M.; Ishimoto, K. Multi-Magnetic-Mode in $(Cr_{1-x}Mn_x)_2As$. *J. Phys. Chem. Solids* **1999**, *60*, 1229–1231.

[26] Yuzuri, M. On the Magnetic Properties of Cr_2As and Cu_2Sb. *J. Phys. Soc. Jpn.* **1960**, *15*, 2007–2012.

[27] Möller, M. H.; Jeitschko, W. The Crystal Structures of Mn_3As_2(II) and Mn_5As_4 Determined from Intergrown Crystals. *Z. Kristallogr.* **1993**, *204*, 77–87.

[28] Hagedorn, M. F.; Jeitschko, W. The Crystal Structure of Mn_3As_2(III). *J. of Solid State Chem.* **1994**, *113*, 257–260.

[29] Dietrich, L. H.; Jeitschko, W.; Möller, M. H. The Crystal Structure of Mn_3As_2(I). *Z. Kristallogr.* **1990**, *190*, 259–269.

[30] Yuzuri, M.; Yamada, M. On the Magnetic Properties of the Compound Mn_2As. *J. Phys. Soc. Jpn.* **1960**, *15*, 1845.

[31] Ishimoto, K.; Okonogi, M.; Ohoyama, K.; Nakajima, K.; Ohashi, M.; Yamauchi, H.; Yamaguchi, Y.; Funahashi, S. Anisotropic Exchange Interaction in Cr_2As. *Phys. B (Amsterdam, Neth.)* **1995**, *213*, 336–338.

[32] Kresse, G.; Marsman, M.; Furthmuller, J. *VASP the Guide*, Institut fur Materialphysik, Universitat Wien. Wien, Austria. Available: http://cms.mpi.univie.ac.at/VASP (accessed Feb. 13, 2012), 2009.

[33] Hafner, J. Ab-Initio Simulations of Materials Using VASP: Density-Functional Theory and Beyond. *J. Comput. Chem.* **2008**, *29*, 2044–2078.

[34] Hobbs, D.; Kresse, G.; Hafner, J. Fully Unconstrained Noncollinear Magnetism within the Projector Augmented-Wave Method. *Phys. Rev. B* **2000**, *62*, 11556–11570.

[35] Dronskowski, R.; Bloechl, P. Crystal Orbital Hamilton Populations (COHP): Energy-Resolved Visualization of Chemical Bonding in Solids Based on Density-Functional Calculations. *J. Phys. Chem.* **1993**, *97*, 8617–8624.

[36] Jepsen, O.; Anderson, O. K. *The Stuttgart TB-LMTO-ASA Program*, version 47; 2000.

[37] Andersen, O. K. Linear Methods in Band Theory. *Phys. Rev. B* **1975**, *12*, 3060–3083.

[38] Momma, K.; Izumi, F. VESTA 3 for Three-Dimensional Visualization of Crystal, Volumetric and Morphology Data. *J. Appl. Crystallogr.* **2011**, *44*, 1272–1276.

[39] FIZ Karlsruhe, *FindIt*; 2012.

[40] Fruchart, D. Electronegative Effects and Metallic Interactions in Ternary Phosphides and Arsenides of Metal-Rich Compounds of Transition Metals. *Proceedings of the VII International Conference on Solid Compounds of Transition Elements*, Grenoble, France, 1982; p PLIII5.

[41] Aroyo, M. I.; Perez-Mato, J. M.; Capillas, C.; Kroumova, E.; Ivantchev, S.; Madariaga, G.; Kirov, A.; Wondratschek, H. Bilbao Crystallographic Server: I. Databases and Crystallographic Computing Programs. *Z. Kristallogr.* **2006**, *221*, 15–27.

[42] Aroyo, M. I.; Kirov, A.; Capillas, C.; Perez-Mato, J. M.; Wondratschek, H. Bilbao Crystallographic Server. II. Representations of Crystallographic Point Groups and Space Groups. *Acta Crystallogr., Sect. A: Found. Crystallogr.* **2006**, *62*, 115–128.

[43] Aroyo, M. I.; Perez-Mato, J. M.; Orobengoa, D.; Tasci, E.; de la Flor, G.; Kirov, A. Crystallography Online: Bilbao Crystallographic Server. *Bulg. Chem. Comm.* **2011**, *43*, 183–197.

[44] Hoffmann, R. A Chemical and Theoretical Way to Look at Bonding on Surfaces. *Rev. Mod. Phys.* **1988**, *60*, 601–628.

[45] Hoffmann, R. How Chemistry and Physics Meet in the Solid State. *Angew. Chem., Int. Ed.* **1987**, *26*, 846–878.

[46] Landrum, G.; Dronskowski, R. Ferromagnetism in Transition Metals: A Chemical Bonding Approach. *Angew. Chem., Int. Ed.* **1999**, *38*, 1389–1393.

[47] Samolyuk, G. D.; Miller, G. J. Relation between Chemical Bonding and Exchange Coupling Approaches to the Description of Ordering in Itinerant Magnets. *J. Comput. Chem.* **2008**, *29*, 2177–2186.

[48] Fokwa, B. P. T.; Samolyuk, G.; Miller, G. J.; Dronskowski, R. Ladders of a Magnetically Active Element in the Structure of the Novel Complex Boride $Ti_9Fe_2Ru_{18}B_8$: Synthesis, Structure, Bonding, and Magnetism. *Inorg. Chem.* **2008**, *47*, 2113–2120.

[49] Brgoch, J.; Goerens, C.; Fokwa, B. P. T.; Miller, G. J. Scaffolding, Ladders, Chains, and Rare Ferrimagnetism in Intermetallic Borides: Electronic Structure Calculations and Magnetic Ordering. *J. Am. Chem. Soc.* **2011**, *133*, 6832–6840.

[50] Austin, A. E.; Adelson, E.; Cloud, W. H. Magnetic Structures of Mn_2As and $Mn_2Sb_{0.7}As_{0.3}$. *J. Appl. Phys.* **1962**, *33*, 1356.

[51] Fokwa, B. P. T.; von Appen, J.; Dronskowski, R. Synthesis of a Missing Structural Link: the First Trigonal Planar B_4 Units in the Novel Complex Boride $Ti_{1+x}Os_{2-x}RuB_2$ ($x = 0.6$). *Chem. Commun. (Cambridge, U. K.)* **2006**, 4419–4421.